Research Square

Preprints are preliminary reports that have not undergone peer review.
They should not be considered conclusive, used to inform clinical practice,
or referenced by the media as validated information.

Iron L-shell opacity measurements under solar convection zone conditions

Qiang Yi

yiqiang@caep.cn

Institute of Nuclear Physics and Chemistry, China Academy of Engineering Physics

Fan Ye

Institute of Nuclear Physics and Chemistry, China Academy of Engineering Physics

Guanqiong Wang

Institute of Applied Physics and Computational Mathematics

Delong Xiao

Institute of Applied Physics and Computational Mathematics

Zeqing Wu

Institute of Applied Physics and Computational Mathematics

Jian Lu

Institute of Nuclear Physics and Chemistry, China Academy of Engineering Physics

Shijian Meng

Institute of Nuclear Physics and Chemistry, China Academy of Engineering Physics

Xiaosong Yan

Institute of Nuclear Physics and Chemistry, China Academy of Engineering Physics

Shuqing Jiang

Institute of Nuclear Physics and Chemistry, China Academy of Engineering Physics

Faxin Chen

Institute of Nuclear Physics and Chemistry, China Academy of Engineering Physics

Jianlun Yang

Institute of Nuclear Physics and Chemistry, China Academy of Engineering Physics

Jiamin Ning

Institute of Nuclear Physics and Chemistry, China Academy of Engineering Physics

Dongming Wang

Institute of Nuclear Physics and Chemistry, China Academy of Engineering Physics

Zeping Xu

Institute of Nuclear Physics and Chemistry, China Academy of Engineering Physics

Haibo You

Institute of Nuclear Physics and Chemistry, China Academy of Engineering Physics

Faqiang Zhang

Institute of Nuclear Physics and Chemistry, China Academy of Engineering Physics

Zhenghong Li
Institute of Nuclear Physics and Chemistry, China Academy of Engineering Physics

Xianbin Huang
Key Laboratory of Pulsed Power, Institute of Fluid Physics, China Academy of Engineering Physics

Xu Qiang
China Academy of Engineering Physics

Shaotong Zhou
Key Laboratory of Pulsed Power, Institute of Fluid Physics, China Academy of Engineering Physics

Daoyuan Zhang
Key Laboratory of Pulsed Power, Institute of Fluid Physics, China Academy of Engineering Physics

Siqun Zhang
Key Laboratory of Pulsed Power, Institute of Fluid Physics, China Academy of Engineering Physics

Xiaodong Ren
Key Laboratory of Pulsed Power, Institute of Fluid Physics, China Academy of Engineering Physics

Ce Ji
Key Laboratory of Pulsed Power, Institute of Fluid Physics, China Academy of Engineering Physics

Yong Li
Key Laboratory of Pulsed Power, Institute of Fluid Physics, China Academy of Engineering Physics

Potao Cai
Key Laboratory of Pulsed Power, Institute of Fluid Physics, China Academy of Engineering Physics

Ji Ren
Key Laboratory of Pulsed Power, Institute of Fluid Physics, China Academy of Engineering Physics

Shi Chen
Key Laboratory of Pulsed Power, Institute of Fluid Physics, China Academy of Engineering Physics

Haoyu Zhang
Key Laboratory of Pulsed Power, Institute of Fluid Physics, China Academy of Engineering Physics

Xiuwen Zhou
Research Center of Laser Fusion, China Academy of Engineering Physics

---

Article

Keywords:

Posted Date: November 17th, 2026

DOI: https://doi.org/10.21203/rs.3.rs-10907742/v1

License: This work is licensed under a Creative Commons Attribution 4.0 International License.
Read Full License

Additional Declarations: There is **NO** Competing Interest.

Iron L-shell opacity measurements under solar convection zone conditions

Qiang Yi[1,2*], Fan Ye[1,2*], Guanqiong Wang[3*], Delong Xiao[3], Zeqing Wu[3], Jian Lu[1,2], Shijian Meng[1,2], Xiaosong Yan[1,2], Shuqing Jiang[1,2], Faxin Chen[1,2], Jianlun Yang[1,2], Jiamin Ning[1,2], Dongming Wang[1,2], Zeping Xu[1,2], Haibo You[1,2], Faqiang Zhang[1,2], Zhenghong Li[1,2], Xianbin Huang[4], Qiang Xu[4], Shaotong Zhou[4], Daoyuan Zhang[4], Siqun Zhang[4], Xiaodong Ren[4], Ce Ji[4], Yong Li[4], Potao Cai[4], Ji Ren[4], Shi Chen[4], Haoyu Zhang[4], Xiuwen Zhou[5]

[1] Institute of Nuclear Physics and Chemistry, China Academy of Engineering Physics, Mianyang, 621900, China .

[2] National Key Laboratory of Neutron Science and Technology, Mianyang, 621900, China .

[3] Institute of Applied Physics and Computational Mathematics, Beijing, 100088, China .

[4] Key Laboratory of Pulsed Power, Institute of Fluid Physics, China Academy of Engineering Physics, Mianyang, 621900, China .

[5] Research Center of Laser Fusion, China Academy of Engineering Physics, Mianyang, 621900, China .

*Corresponding author(s). E-mail(s): yiqiang@caep.cn; yefan1931@126.com; wangguanqiong@caep.cn;

Abstract

We report spectrally resolved measurements of iron $\boldsymbol{L}$-shell opacity in a high-energy-density plasma produced by a Z-pinch dynamic hohlraum. An Fe/Al mixed sample is volumetrically heated by a $\sim$ **6** ns quasi-Planckian x-ray drive and probed by a $\sim$ **2** ns backlighter pulse, both generated by the dynamic hohlraum, with the backlighter radiation at stagnation. Simultaneous single-shot measurements of Fe $\boldsymbol{L}$-shell and Al $\boldsymbol{K}$-shell absorption spectra provide self-consistent plasma diagnostics, yielding plasma conditions near $\boldsymbol{T_e = 115}$ eV

and $\boldsymbol{n_e = 1.4 \times 10^{22}}$ $\mathbf{cm^{-3}}$. The Fe $\boldsymbol{L}$-shell opacity is determined from the measured transmission and compared with DCA–UTA and PrismSPECT calculations. These measurements open a new experimental window for opacity studies in the previously unexplored 100–150 eV hot-dense-matter regime relevant to stellar interiors.

Opacity quantifies the interaction between radiation and matter and is a fundamental property governing energy transport in high-energy-density (HED) plasmas relevant to inertial confinement fusion (ICF), stellar interiors, and laboratory radiation sources[1–5]. In ICF, opacity determines how x-ray radiation is absorbed and transported through the target, thereby shaping energy deposition and implosion dynamics and affecting the predictive accuracy of radiation-hydrodynamic simulations and target designs. In stellar interiors, opacity controls the transport of energy generated in stellar cores and is essential for reliable models of stellar structure and evolution. Discrepancies between standard solar models and helioseismic observations have been linked to possible inaccuracies in opacity calculations under solar-interior conditions[4,6].

Stellar structure and evolution depend critically on the transport of energy from nuclear-burning cores through different interior layers. Fig. 1 illustrates the temperature and density profiles of the solar interior from the standard solar Model S[7]. The radiative and convective zones of the Sun span a broad range of partially ionized plasma conditions ($T_e \sim$ 100–700 eV), where accurate opacity data are essential for reliable stellar modeling[1]. Despite substantial progress in reproducing stellar-interior conditions in laboratory experiments, experimental opacity benchmarks remain limited over this parameter space, where different atomic models can exhibit significant discrepancies.

Iron (Fe), despite its relatively low abundance compared with H and He in stellar plasmas, is among the dominant contributors to the Rosseland mean opacity, together with carbon, oxygen and neon[1,8], because of its dense manifold of bound-bound and bound-free transitions[1,9,10]. At electron temperatures of order 10^2 eV, Fe retains open L-shell configurations, producing extensive transition arrays that strongly influence opacity. Bailey *et al.*[11] measured Fe opacity under conditions representative of the solar radiative–convective boundary (T_e = 160–200 eV, $n_e = (0.7\text{–}4.0) \times 10^{22}$ cm^{-3}), reporting measured opacities 30%–400% higher than theoretical predictions. More recently, Loisel *et al.*[12] demonstrated that temporal gradients cannot account for these discrepancies, indicating unresolved challenges in opacity modeling. However, experimental Fe-opacity data remain scarce at $T_e \sim$ 100–150 eV, a regime characteristic of the solar convection zone. Measurements in this regime are therefore critical for testing atomic-physics models and improving radiation-transport calculations in astrophysical and HED plasmas.

Opacity measurements in HED plasmas typically rely on backlighting techniques. Laser-driven point-projection geometries provide high spatial resolution but often involve structured backlighter spectrum that complicate spectral interpretation. In contrast, pulsed-power-driven Z-pinch dynamic hohlraums (ZPDH) provide quasi-continuum backlighting and volumetric heating, offering advantages for opacity

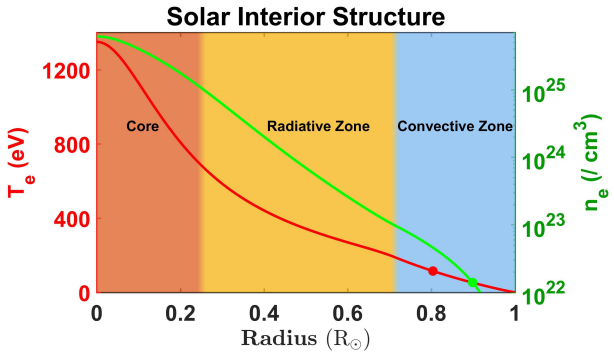


Fig. 1 The electron temperature (red) and electron density (green) in the Sun's interior according to the standard solar Model S[7]. The dot indicates the plasma temperature and density for the opacity measurement here.

measurements under HED and near-local-thermodynamic-equilibrium (LTE) conditions. Unlike laser-driven platforms, where plasma heating and backlighting can be independently tailored, a ZPDH intrinsically couples these two processes through the implosion dynamics, requiring careful optimization of the target and diagnostic configuration for opacity measurements.

A central challenge in opacity experiments is to simultaneously achieve high temperature, high density, and sufficient plasma uniformity. Longer radiative heating promotes temperature equilibration but also drives hydrodynamic expansion, requiring a balance between plasma heating and sample evolution. The backlighter pulse must remain short relative to the hydrodynamic evolution time to preserve well-defined plasma conditions during the transmission measurement[13]. In addition, simultaneous determination of plasma conditions and opacity requires tracer elements such as Al or Mg[9,14,15], whose well-known K-shell absorption features must be measured together with the weaker Fe L-shell absorption within the available spectral range and instrumental resolution.

In this work, we report spectrally resolved measurements of Fe L-shell opacity using a ZPDH platform on an 8-MA pulsed-power facility. An Fe/Al mixed sample is volumetrically heated and backlighted by the ZPDH radiation source, and the absorption spectrum is recorded using an elliptically bent crystal spectrometer that simultaneously captures Fe L-shell and Al K-shell absorption features, with the Al K-shell absorption providing in situ plasma diagnostics and the Fe L-shell transmission is used to infer the opacity.

Results

Radiation-hydrodynamic optimization of the opacity sample

Fig. 2 shows that the Fe/Al-layer-thickness-weighted average plasma temperature and density at the time of backlighting depend primarily on the radiation temperature and only weakly on the total sample areal density varied through different Fe/Al thickness combinations. Here, the thickness values denote designed Fe/Al layer thickness pairs

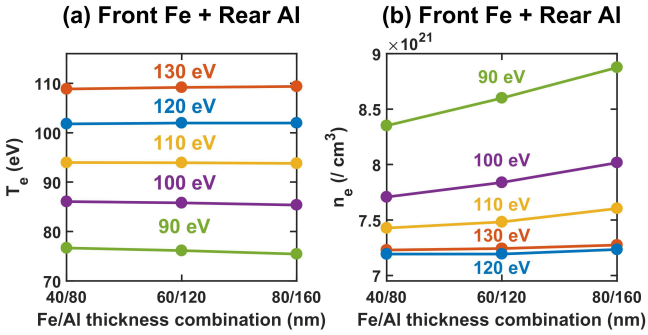


Fig. 2 Fe/Al-layer-thickness-weighted average (a) electron temperature, T_e, and (b) electron density, n_e, at the time of backlighting for the CH/Fe(60 nm)/Al(120 nm)/CH configuration used in the measurement (middle point), together with two neighboring Fe/Al thickness combinations (40/80 and 80/160 nm). The results are computed for five peak radiation temperatures, T_r, ranging from 90 to 130 eV.

rather than spatial positions within the sample. The sample temperature is determined by the balance between x-ray radiative heating and energy losses through re-emission and expansion, rather than by exact thermal equilibrium with the drive, and remains about 20 eV below the source radiation temperature. For the reversed layer sequence Al(120 nm)/Fe(60 nm) the results are nearly identical and are not shown.

Fig. 3 compares the plasma uniformity for different radiation temperatures, Fe/Al thickness combinations, and layer sequences. For the selected CH/Fe(60 nm)/Al(120 nm)/CH configuration, the calculated nonuniformities remain small, with $\Delta T_\mathrm{e} \approx 6$ eV and $\Delta n_\mathrm{e}/n_\mathrm{e} \approx 7\%$ at $T_\mathrm{r} = 130$ eV. Increasing the Fe/Al layer thickness increases the temperature and density differences, while the CH/Fe/Al/CH configuration exhibits slightly better uniformity than CH/Al/Fe/CH, particularly at lower radiation temperatures. This behavior reflects the interplay between radiation deposition and subsequent plasma equilibration. With Fe facing the radiation source, its stronger absorption modifies the radiation field incident on the Al layer, resulting in a more balanced energy deposition across the Fe/Al stack. Reversing the layer sequence leads to a substantially larger deposition contrast between the Fe and Al layers. The smaller initial energy imbalance in the Fe-front configuration results in reduced temperature and density gradients after subsequent collisional energy exchange and hydrodynamic evolution. The two configurations are therefore considered limiting cases for axial heating asymmetry rather than exact representations of the fabricated sample. In addition, the sample remains close to LTE during the opacity measurement, as verified by the electron, ion, and radiation temperature differences remaining within 2 eV over the interval from -2.9 to -1.7 ns surrounding the peak backlight, as shown in Fig. 4.

Based on the radiation-hydrodynamic optimization described above, the fabricated opacity sample closely follows the optimized configuration and consists of CH(2 μm)/Fe(60 nm)+Al(120 nm)/CH(8 μm). The central absorption layer is a homogeneous Fe–Al mixture with an atomic ratio of 0.7:1 deposited by magnetron sputtering, corresponding to Fe and Al areal mass densities of 0.0468 and

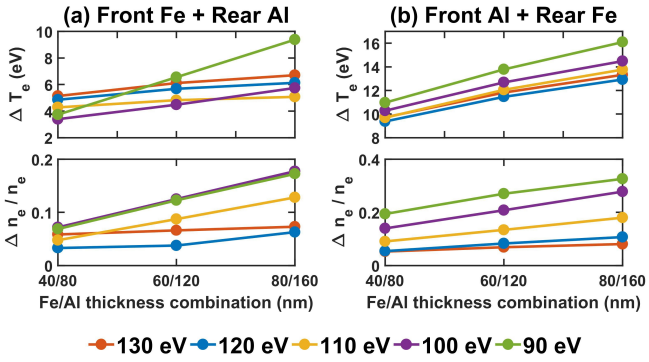


Fig. 3 Fe/Al-Layer-thickness-weighted average electron temperature differences, ΔT_e, and relative electron density differences, $\Delta n_e/n_e$, evaluated across the Fe/Al layer for (a) the CH/Fe/Al/CH configuration and (b) the CH/Al/Fe/CH configuration. The results are shown for Fe/Al thickness combinations of 40/80, 60/120, and 80/160 nm at drive source radiation temperatures of 90–130 eV.

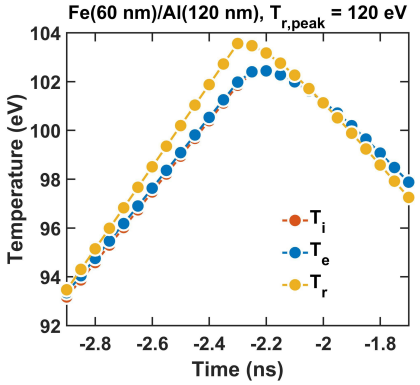


Fig. 4 Validation of the local thermodynamic equilibrium (LTE) assumption through comparison of the electron (T_e), ion (T_i), and radiation (T_r) temperatures for the CH/Fe (60 nm)/Al (120 nm)/CH configuration. The backlight peaks at −2.3 ns, with zero time defined as the moment of peak radial power.

0.0324 mg/cm^2, respectively, equivalent to effective thicknesses of 60 and 120 nm for bulk Fe and Al.

Simultaneous measurement of Fe L-shell and Al K-shell absorption

To evaluate the feasibility of the transmission measurement, the Al K-shell and Fe L-shell transmission spectra at the peak backlight time (−2.3 ns) are calculated using the detailed-level accounting (DLA) model[16,17] and the detailed configuration accounting–unresolved transition array (DCA–UTA) model[18,19], respectively, and convolved with a Gaussian instrumental response. During this calculation, the Fe/Al thickness has been optimized to achieve an optical depth near unity ($T \sim e^{-1}$), providing strong yet

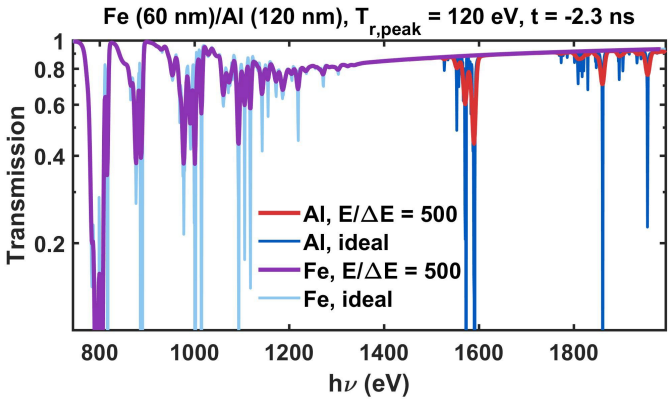


Fig. 5 Synthetic transmission at the peak backlight time (−2.3 ns) for the CH/Fe (60 nm)/Al (120 nm)/CH configuration after Gaussian convolution with an instrumental resolving power of $E/\Delta E = 500$. The purple and light-blue curves correspond to Fe L-shell transmission, while the red and dark-blue curves represent Al K-shell transmission before and after instrumental broadening, respectively.

unsaturated absorption features for sensitive opacity diagnostics. The calculated transmission as a function of photon energy $h\nu$ for the CH/Fe (60 nm)/Al (120 nm)/CH target configuration is shown in Fig. 5. After convolution with an instrumental resolving power of $E/\Delta E = 500$, the dominant Fe L-shell and Al K-shell absorption structures remain clearly identifiable.

Fig. 6 shows the absorption spectrum obtained from shot 1099, one of the two shots in the experimental campaign that most clearly resolves both the Fe L-shell and Al K-shell absorption features, with a resolving power of $E/\Delta E > 800$ at the Al He-α line and a signal-to-noise ratio of approximately 5:1. The spectrum resolves Fe L-shell absorption structures between 970 and 1300 eV, together with the Al K-shell He-series and Li-like satellite features used for plasma diagnostics. A weak absorption feature near 1823 eV is also observed, consistent with tungsten absorption from dynamic-hohlraum wire-array mix reported previously on the 8-MA platform[15,20] and in Sandia Saturn experiments[21].

Discussion

Self-consistent plasma diagnostics

The transmission is obtained by dividing the absorption spectrum in Fig. 6(b) by a reference backlighter spectrum measured previously under nominally identical experimental conditions[15]. Comparison of the measured Al K-shell transmission in Fig. 7(a) with calculations from the DLA model and the PrismSPECT code[22,23] shows good agreement in the positions, widths and relative strengths of the major absorption features, including the Li-like satellite near 1577 eV and the He-α, He-β, and He-γ transitions. This agreement constrains the plasma conditions to $T_e = 115$ eV and

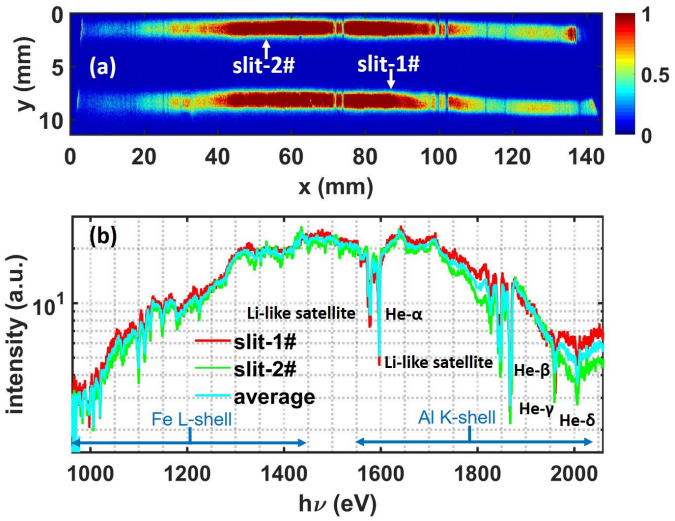


Fig. 6 (a) Absorption spectral image, from shot 1099, showing dense Fe L-shell and characteristic Al K-shell absorption features. The lower and upper images correspond to slit #1 and slit #2, respectively. Horizontal and vertical scales are different for clarity. (b) Corresponding lineouts obtained by vertically integrating the central 1 mm region of the spectral image in (a), from which the Fe L-shell and Al K-shell absorption spectrum are extracted.

$n_e = 1.4 \times 10^{22}$ cm^{-3}. Assuming conservation of areal density during tamped expansion, these conditions correspond to a mass density of approximately 6×10^{-2} g cm^{-3}, consistent with radiation-hydrodynamic simulations. An additional absorption feature near 1850 eV, absent from the LTE DLA calculations, is identified as Li-like Al satellite absorption arising from excited configurations, according to the PrismSPECT atomic database and the NIST Atomic Spectra Database Levels Data. This feature originates from excited-state populations and remains separated from the principal Al K-shell absorption structures employed for the temperature and density determination.

Multi-charge-state modeling of Fe L-shell transmission

Using the plasma conditions inferred from the Al K-shell diagnostics, the Fe and Al charge-state distributions were calculated with PrismSPECT and are shown in Fig. 8. The Al charge-state distribution is concentrated around Al XII, with significant contributions from Al X to Al XII, whereas the Fe distribution extends from Fe XIII to Fe XIX and peaks at Fe XVI. The corresponding mean ionization states are $\langle Z \rangle =$ 10.49 for Al and 15.24 for Fe. The relatively localized Al charge-state distribution facilitates the use of Al K-shell absorption features for plasma diagnostics, while the broader Fe charge-state distribution results in the complex L-shell absorption manifold observed in the transmission.

Using these plasma conditions, the Fe L-shell transmission was calculated with DCA–UTA and PrismSPECT. After instrumental broadening ($E/\Delta E$ = 500–800), the DCA–UTA calculation reproduces the measured absorption spectrum well, including the positions, width and relative strengths of prominent features associated with

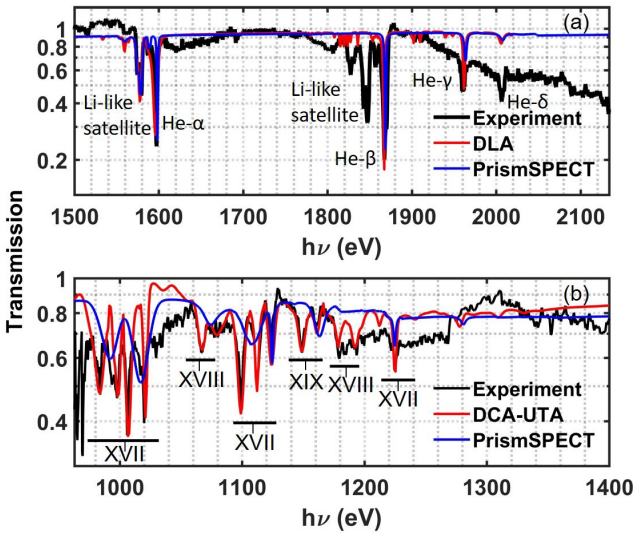


Fig. 7 (a) Measured Al K-shell transmission with DLA and PrismSPECT fits used to infer the plasma temperature and density. (b) Fe L-shell transmission compared with DCA–UTA and PrismSPECT calculations based on the inferred plasma conditions.

the $2p$–$3d$, $2p$–$4d$, and $2p$–$5d$ transition arrays of Fe^{16+}–Fe^{18+} ions [Fig. 7(b)]. PrismSPECT also reproduces the overall Fe L-shell absorption structure and spectral envelope, although some individual features appear broadened or shifted relative to the DCA–UTA result. These differences arise from the extremely dense and overlapping transition manifolds in partially ionized Fe, where multiple configurations and charge states contribute simultaneously to the measured absorption. The DCA–UTA approach explicitly resolves a larger number of configuration-dependent transition arrays, whereas the statistical treatment adopted in PrismSPECT represents groups of strongly overlapping transitions in a more averaged manner. Consequently, individual spectral features may be represented differently, while the dominant absorption envelope and overall opacity behavior remain consistent between the two calculations. Both calculations therefore support the interpretation of the measured Fe L-shell transmission and the extracted opacity under the diagnosed plasma conditions.

Transmission-derived Fe L-shell opacity under stellar-interior conditions

The transmission is related to opacity through the Beer–Lambert law

$$T(h\nu) = \exp[-\kappa(h\nu)\rho L], \tag{1}$$

where $\kappa(h\nu)$ and ρL denote the opacity and sample areal density, respectively. Assuming conserved areal density, the Fe opacity extracted from the measured transmission spectrum is shown in Fig. 9, together with DCA–UTA and PrismSPECT calculations.

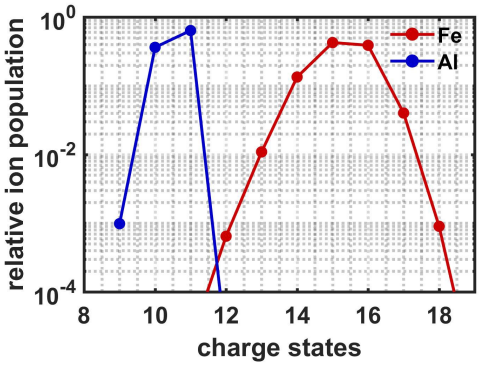


Fig. 8 Calculated charge-state distributions of Fe and Al under the inferred plasma conditions of $T_e = 115$ eV and $n_e = 1.4 \times 10^{22}$ cm^{-3}.

The measured opacity is dominated by broad Fe L-shell absorption complexes produced by overlapping $2p$–nd transition arrays ($n = 3, 4, 5, \ldots$) from partially ionized Fe ions. Under the diagnosed plasma conditions, the DCA–UTA calculation reproduces the spectral distribution and magnitude of the dominant opacity structures, reflecting its explicit treatment of configuration-dependent transition arrays. The PrismSPECT calculation also captures the overall opacity envelope and the redistribution of absorption strength across the measured energy range, although individual spectral modulations appear smoother and some local maxima differ from those predicted by DCA–UTA. These differences arise from the distinct treatments of the highly dense transition manifold in partially ionized Fe plasmas. DCA–UTA resolves a larger number of configuration-dependent contributions, whereas PrismSPECT represents strongly overlapping transitions from multiple charge states and configurations through a statistical approach that emphasizes the averaged spectral behavior. Consequently, individual spectral features may be redistributed differently between the two calculations, while the dominant opacity scale and broad absorption characteristics remain consistent. This agreement indicates that the extracted Fe L-shell opacity reflects the underlying absorption behavior of the plasma within the present experimental resolution.

In summary, we report spectrally resolved measurements of Fe L-shell opacity in the 970–1300 eV range on an 8-MA pulsed-power ZPDH platform. The simultaneous single-shot measurement of Fe L-shell and Al K-shell absorption spectra enables self-consistent plasma diagnostics and Fe-opacity determination at $T_\mathrm{e} = 115$ eV and $n_\mathrm{e} = 1.4 \times 10^{22}\,\mathrm{cm}^{-3}$. The measured opacity is broadly consistent with both DCA–UTA and PrismSPECT calculations at the level of the overall spectral envelope and magnitude, while DCA–UTA provides a more detailed description of the dominant spectral structures. By establishing experimental access to Fe-opacity measurements in the largely unexplored 100–150 eV temperature regime, this work provides a benchmark for testing the treatment of dense, overlapping transition arrays in partially ionized Fe and for improving opacity calculations relevant to stellar interiors and HED radiation transport.

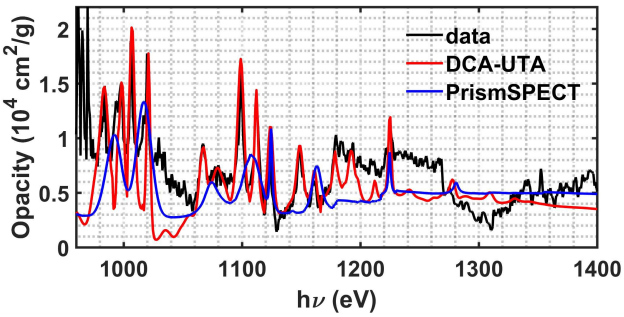


Fig. 9 Experimental Fe opacity inferred from the measured transmission under the conserved areal density assumption, compared with DCA-UTA and PrismSPECT calculations at plasma conditions of $T_e = 115$ eV and $n_e = 1.4 \times 10^{22}$ cm^{-3}. The dominant absorption structures arise primarily from Fe L-shell $2p - 3d$, $2p - 4d$ and $2p - 5d$ transitions.

Methods

Radiation-hydrodynamic simulations

One-dimensional radiation-hydrodynamic simulations are performed using the RDMG code[24,25] to optimize the opacity sample and characterize its evolution under x-ray drive, including the layer-thickness-weighted plasma conditions, spatial uniformity, and LTE behavior required for reliable opacity measurements[26]. The experimentally measured end-on radiation-temperature waveform from shot 0788, with a peak temperature of approximately 130 eV[15,20], is used as the radiation-drive boundary condition. Although the fabricated Fe/Al sample is physically mixed, two limiting layered configurations, CH/Fe/Al/CH and CH/Al/Fe/CH, corresponding to iron or aluminum being closer to the radiation source, respectively, are considered to bound possible axial asymmetries in the radiative heating. The CH tampers suppress rarefaction, allowing the sample areal density to remain approximately constant during the backlighting interval.

To optimize the sample design, five radiation temperatures (90–130 eV) and three Fe/Al thickness combinations [Fe(40, 60, 80 nm)/Al(80, 120, 160 nm)] are simulated. A fixed Fe:Al thickness ratio of 1:2, determined through experimental optimization and radiation-hydrodynamic simulations, is adopted to provide adequate transmission contrast for both Al plasma diagnostics and Fe-opacity measurements. Layer-thickness-weighted plasma conditions, temperature and density nonuniformities, and the approach to LTE are evaluated at the time of backlighting.

Atomic-physics calculations

The Al K-shell absorption spectrum was calculated using the DLA model[16,17], which treats individual atomic levels and transitions to provide detailed spectral structures. The Fe L-shell absorption spectrum was calculated using the DCA–UTA model[18,19], which combines configuration-level accounting with statistical treatment of dense unresolved transition arrays and is suitable for describing the complex absorption features arising from multiple partially ionized Fe charge states.

PrismSPECT[22,23] was used as an independent collisional-radiative spectral modeling tool to calculate ionization distributions, atomic populations, and absorption spectra under the diagnosed plasma conditions, considering either LTE or non-LTE conditions. The PrismSPECT calculations were compared with the experimental Al K-shell and Fe L-shell absorption spectra, together with the corresponding DLA and DCA–UTA calculations, respectively. All calculated spectra were convolved with the instrumental response before comparison with the experimental measurements.

Absorption spectrum diagnostic

A slit array coupled to a potassium acid phthalate (KAP) elliptical curved-crystal spectrometer was designed and implemented using ray-tracing optimization of the focusing geometry. The design provides an effective energy coverage of approximately 900–2100 eV and a source-broadening-limited resolving power of $E/\Delta E > 1000$, enabling simultaneous measurement of the Fe L-shell and Al K-shell absorption features. Further details of the diagnostic design are given in Ref. 15.

Extraction of Fe-only transmission and opacity

The transmission was obtained by normalizing the sample-attenuated spectrum to a reference backlighter spectrum acquired under nominally identical experimental conditions[15]. For the Fe/Al mixed sample, the measured transmission contains contributions from both Fe L-shell and Al K-shell absorption. The Fe L-shell contribution was separated from the mixed Fe/Al transmission by removing the PrismSPECT-calculated Al transmission based on the diagnosed plasma conditions, yielding the Fe-only transmission. The Fe L-shell opacity was then extracted from the Fe-only transmission according to

$$\kappa(h\nu) = -\frac{\ln[T_{\mathrm{Fe}}(h\nu)]}{\rho_{\mathrm{Fe}} L}, \tag{2}$$

where $\rho_{\mathrm{Fe}} L$ denotes the Fe areal density of the sample.

Data Availability

The data supporting the findings of this study have been deposited in the Figshare repository and will be made publicly available upon publication.

Code Availability

The analysis codes developed in this study for ray tracing and experimental data processing are available from the corresponding authors upon reasonable request. Radiation-hydrodynamics and atomic physics calculations were performed using internally developed codes, including RDMG, DLA, and DCA–UTA, whose distribution is restricted. The PrismSPECT calculations were performed using licensed software, and its availability is subject to the respective developers' policies.

References

1. Rogers, F. J. & Iglesias, C. A. Astrophysical Opacity. *Science* **263**, 50 (1994).

2. McWilliams, R. S., Dalton, D. A., Konôpková, Z., Mahmood, M. F. *et al.* Opacity and conductivity measurements in noble gases at conditions of planetary and stellar interiors. *Proc. Natl. Acad. Sci. USA* **112**, 7925–7930 (2015).

3. Wang, P., MacFarlane, J. J. & Orzechowski, T. J. An investigation of the opacity of high-Z mixture and implications for inertial confinement fusion hohlraum design. *Rev. Sci. Instrum.* **68**, 1107 (1997).

4. Basu, S. & Anitia, H. M. Helioseismology and solar abundances. *Phys. Rep.* **457**, 217 (2008).

5. Fujioka, S., Nishimura, H., Nishihara, K., Sasaki, A. *et al.* Opacity Effect on Extreme Ultraviolet Radiation from Laser-Produced Tin Plasmas. *Phys. Rev. Lett.* **95**, 235004 (2005).

6. Delahaye, F. & Pinsonneault, M. Comparison of radiative accelerations obtained with atomic data from OP and OPAL. *Astrophys. J.* **625**, 563 (2005).

7. Christensen-Dalsgaard, J., Däppen, W., Ajukov, S. V., Anderson, E. R. *et al.* The current state of solar modeling. *Science* **272**, 1286–1292 (1996).

8. Bailey, J. E., Mayes, D. C., Loisel, G. P., Nagayama, T. *et al.* Oxygen opacity measurements at high-energy-density conditions. *Phys. Rev. Lett.* **135**, 205101 (2025).

9. Bailey, J. E. *et al.* Experimental investigation of opacity models for stellar interior, inertial fusion, and high energy density plasmas. *Phys. Plasmas* **16**, 058101 (2009).

10. Whittaker, D. S. & Tallents, G. J. Iron opacity predictions under solar interior conditions. *Mon. Not. R. Astron. Soc.* **400**, 1808–1813 (2009).

11. Bailey, J. E., Nagayama, T., Loisel, G. P., Rochau, G. A. *et al.* A higher-than-predicted measurement of iron opacity at solar interior temperatures. *Nature* **517**, 56 (2015).

12. Loisel, G. P., Bailey, J. E., Nagayama, T., Hansen, S. B. *et al.* First measurement of z opacity sample evolution near solar interior conditions using time-resolved spectroscopy. *Phys. Rev. Lett.* **134**, 095101 (2025).

13. Nagayama, T. *et al.* Calibrated simulations of z opacity experiments that reproduce the experimentally measured plasma conditions. *Phys. Rev. E* **93**, 023202 (2016).

14. Perry, T. S., Springer, P. T., Fields, D. F., Bach, D. R. *et al.* Absorption experiments on x-ray-heated mid-Z constrained samples. *Phys. Rev. E* **54**, 5617 (1996).

15. Yi, Q., Ye, F., Lu, J., Yan, X. *et al.* Ionization dynamics and x-ray transmission of aluminum plasma at temperature reaching 110 ev. *Phys. Rev. E* **110**, 065205 (2024).

16. Han, X., Bao, L., Zhang, H., Liu, C. *et al.* Atomic Data and Their Application in Calculation of Plasma Radiative Properties. *AIP Conf. Proc.* **1344**, 188 (2011).

17. Zeng, J. & Yuan, J. Radiative opacity of gold plasmas studied by a detailed level-accounting method. *Phys. Rev. E* **74**, 025401(R) (2006).

18. Yan, J. & Li, J. M. Theoretical simulation of the transmission spectra of fe and ge plasmas. *Chinese Physics Letters* **17**, 194–196 (2000).

19. Yan, J. & Wu, Z. Q. Theoretical investigation of the increase in the rosseland mean opacity for hot dense mixtures. *Phys. Rev. E* **65**, 066401 (2002).

20. Yi, Q., Meng, S., Ye, F., Lu, J. *et al.* Initial characterization of a dynamic hohlraum radiation source tailored for high-temperature opacity measurements at an 8-MA facility. *AIP Advances* **13**, 035216 (2023).

21. Nash, T. J., Derzon, M. S., Chandler, G. A., Leeper, R. *et al.* High-temperature dynamic hohlraums on the pulsed power driver Z. *Phys. Plasmas* **6**, 2023 (1999).

22. MacFarlane, J., Golovkin, I., Woodruff, P. *et al.* Simulation of the ionization dynamics of aluminum irradiated by intense short-pulse lasers. *Inertial Fusion Sciences and Application* 457 (2003).

23. Golovkin, I., Gu, M. F., MacFarlane, J., Sebald, J. & Walton, T. Collisional-radiative spectral analysis code prismspect. *High Energy Density Physics* **58**, 101255 (2025).

24. Feng, T. G., Lai, D. X. & Xu, Y. An artificial-scattering iteration method for calculating multi-group radiation transfer problem. *J. Comput. Phys* **16**, 199 (1999). (in Chinese).

25. Meng, G., Wang, J., Wang, X., Li, J. & Zhang, W. Generation of a sharp density increase in radiation transport between high-Z and low-Z plasmas. *Matter Radiat. Extremes* **1**, 249 (2016).

26. Nagayama, T., Bailey, J. E., Loisel, G. P., Dunham, G. S. *et al.* Systematic study of l-shell opacity at stellar interior temperatures. *Phys. Rev. Lett.* **122**, 235001 (2019).

Acknowledgements

The authors sincerely acknowledge the operation crew of the 8-MA pulsed power facility at the Institute of Fluid Physics, the target fabrication team at the Research Center of Laser Fusion, and the Institute of Applied Physics and Computational Mathematics for support with theoretical calculations. The authors also acknowledge Dr. Nino R. Pereira for helpful discussions on plasma theory and diagnostics. This work was supported by the Science Challenge Project (No. TZ2025014) and the National Natural Science Foundation of China (Grant Nos. 12135010, 12175207, 12305227, 12075225, and 12305206).

Author Contributions

Q.Y., F.Y., and G.W. conceived and designed the study. F.Y. and Q.Y. designed and optimized the experiments, with contributions from X.Y. and F.Z. Q.Y. and F.Y. developed and optimized the diagnostic design, which was implemented by S.J., J.Y., J.N., and D.W., with diagnostic control and operation supported by X.H., Q.X., S.Z., D.Z., S.Z., X.R., C.J., Y.L., P.C., J.R., S.C., and H.Z. X.Z. fabricated the experimental targets and samples. G.W. and D.X. performed the radiation-hydrodynamic simulations. G.W. and Z.W. carried out the atomic-physics calculations. Q.Y., F.Y., H.Y., and F.C. analyzed the experimental data. S.M. and J.L. contributed to data visualization. Q.Y., F.Y., and G.W. led the project and coordinated the scientific efforts, with guidance and support from D.X., Z.X., and Z.L. Q.Y. and G.W. wrote the manuscript draft, with contributions from F.Y. All authors discussed the results and contributed to the final manuscript. All authors reviewed and approved the final version of the manuscript.

Competing Interests

The authors declare no competing interests.